JOURNAL OF PETROLOGY | VOLUME 52 | NUMBER 5 | PAGES 891–904 | 2011 | doi:10.1093/petrology/egr008

Molybdenite Saturation in Silicic Magmas: Occurrence and Petrological Implications

ANDREAS AUDÉTAT[1]*, DAVID DOLEJŠ[2] AND JACOB B. LOWENSTERN[3]

[1]BAYERISCHES GEOINSTITUT, UNIVERSITÄT BAYREUTH, 95440 BAYREUTH, GERMANY

[2]INSTITUTE OF PETROLOGY AND STRUCTURAL GEOLOGY, CHARLES UNIVERSITY, 12843 PRAHA 2, CZECH REPUBLIC

[3]VOLCANO SCIENCE CENTER, US GEOLOGICAL SURVEY, 345 MIDDLEFIELD ROAD, MENLO PARK, CA 94025, USA

RECEIVED JULY 28, 2010; ACCEPTED FEBRUARY 14, 2011
ADVANCE ACCESS PUBLICATION MARCH 31, 2011

We identified molybdenite (MoS_2) as an accessory magmatic phase in 13 out of 27 felsic magma systems examined worldwide. The molybdenite occurs as small (<20 μm) triangular or hexagonal platelets included in quartz phenocrysts. Laser-ablation inductively coupled plasma mass spectrometry analyses of melt inclusions in molybdenite-saturated samples reveal 1–13 ppm Mo in the melt and geochemical signatures that imply a strong link to continental rift basalt–rhyolite associations. In contrast, arc-associated rhyolites are rarely molybdenite-saturated, despite similar Mo concentrations. This systematic dependence on tectonic setting seems to reflect the higher oxidation state of arc magmas compared with within-plate magmas. A thermodynamic model devised to investigate the effects of T, fO_2 *and* fS_2 *on molybdenite solubility reliably predicts measured Mo concentrations in molybdenite-saturated samples if the magmas are assumed to have been saturated also in pyrrhotite. Whereas pyrrhotite microphenocrysts have been observed in some of these samples, they have not been observed from other molybdenite-bearing magmas. Based on the strong influence of* fS_2 *on molybdenite solubility we calculate that also these latter magmas must have been at (or very close to) pyrrhotite saturation. In this case the Mo concentration of molybdenite-saturated melts can be used to constrain both magmatic* fO_2 *and* fS_2 *if temperature is known independently (e.g. by zircon saturation thermometry). Our model thus permits evaluation of magmatic* fS_2*, which is an important variable but is difficult to estimate otherwise, particularly in slowly cooled rocks.*

KEY WORDS: *molybdenite; sulfur fugacity; rhyolite; melt inclusions; laser ablation ICP-MS*

INTRODUCTION

Sulfur-rich minerals are a minor but petrogenetically important constituent of intermediate to silicic magmas, providing information about the fugacities of sulfur (fS_2) and oxygen (fO_2) during magmatic crystallization (e.g. Whitney, 1984; Carroll & Webster, 1994), and they control the distribution of chalcophile elements during magma evolution (e.g. Simon *et al.*, 2008). Sulfate minerals, mainly represented by anhydrite (Luhr, 2008), are stable in oxidized magmas ($fO_2 > NiNiO + 0.5$), whereas pyrrhotite and/or immiscible sulfide melts prevail at more reducing conditions (e.g. Carroll & Webster, 1994). The composition of pyrrhotite ($Fe_{1-x}S$) varies as a function of temperature and fS_2, and thus can be used to estimate magmatic fS_2 (e.g. Whitney, 1984), which is a key variable for interpreting the ore-forming processes (e.g. Hedenquist & Lowenstern, 1994) or evaluating climatic impacts of volcanic eruptions (e.g. Rampino & Self, 1992; Briffa *et al.*, 1998).

Magmatic sulfides tend to rapidly decompose in solidifying magmatic rocks and during hydrothermal alteration, and thus are difficult to study unless preserved as inclusions in phenocryst phases. Magmatic pyrrhotite and Cu–Fe sulfide melts have been described from a number of intermediate to felsic rocks in various tectonic settings (e.g. Stimac & Hickmott, 1994; Chesner, 1998; Gardner, 2007; Hildreth & Wilson, 2007). In contrast, molybdenite (MoS_2) is considered a very uncommon magmatic phase, with the only occurrence reported so far being the

*Corresponding author. E-mail: andreas.audetat@uni-bayreuth.de

peralkaline rhyolites from Pantelleria, Italy (Lowenstern *et al.*, 1993). In this study we document the occurrence of magmatic molybdenite in 13 felsic magma systems examined worldwide and explore key variables that control Mo behavior in evolved magmatic systems. We also demonstrate that most (if not all) of these magmas have been additionally saturated in pyrrhotite, which allows magmatic fS_2 and fO_2 to be estimated based on the Mo concentration of the melt.

METHODS

About 50 rhyolitic to dacitic samples were examined from 22 magmatic suites in the western USA and from one each in Alaska, New Zealand, Italy, Indonesia and Eritrea (Table 1 and Electronic Appendix I, available for downloading at http://www.petrology.oxfordjournals.org/). In six of these magmatic suites the studied samples were intrusive rocks, whereas the remaining 21 were volcanic. Four suites (Pine Grove, Cave Peak, Latir Volcanic Field and Treasure Mt. Dome) are genetically related to economic porphyry Mo mineralization. Between 10 and 400 quartz phenocrysts from each sample were studied by optical microscopy in polished thick sections of 0·2–0·8 mm thickness. No other host minerals were studied because they were either less abundant, generally poor in inclusions, or altered. Our primary focus was on opaque to semi-transparent solid inclusions that were fully enclosed by quartz and were not situated along cracks or fluid inclusions trails. Suspected molybdenite inclusions were identified by Raman spectroscopy using a Dilor Raman microprobe with a resolution of 1800 lines per mm, a focal length of 500 mm and a 633 nm wavelength (red) for excitation. Molybdenite shows characteristic Raman bands at ~385, 410 and 424 cm^{-1} and less intense ones at ~532, 575, 604 and 645 cm^{-1} (± a few cm^{-1} owing to potential strain), none of which overlap with the quartz spectrum.

Three to 10 quartz-hosted melt inclusions from each sample (if possible along the same growth zones as the molybdenite inclusions) were analyzed by laser-ablation inductively coupled plasma mass spectrometry (ICP-MS), using a 193 nm Excimer Laser with homogenization optics (GeoLas Pro System, Coherent Inc.) combined with an Elan DRC-e quadrupole mass spectrometer (Perkin Elmer, Canada). Technical descriptions of this system and quantification strategies have been given by, for example, Günther *et al.* (1998), Halter *et al.* (2002), Heinrich *et al.* (2003) and Pettke (2006, 2008). In most cases, entire melt inclusions were drilled out of their host without prior re-homogenization, and their bulk composition was calculated by integrating the resulting signals and subtracting the contribution owing to ablated host.

External standardization was based on NIST SRM 610, using the reference values of the GeoReM database (http://georem.mpch-mainz.gwdg.de), except for Nb for which the reference value of Hu *et al.* (2008) was used. The MPI-DING glasses KL2-G and ATHO-G (Jochum *et al.*, 2006) were periodically analyzed as unknowns (normalizing the sum of major element oxides to 100 wt %) to monitor the quality of the quantification procedure. Calculated average concentrations in these MPI-DING glasses agree with the reference values within 5% relative for all elements significantly above the detection limit, except for Y (−10%) and Zr (−9%) in KL2-G, and Na (+10%), Mg (−10%), Mo (−26%) and Cs (−16%) in ATHO-G.

Internal standardization of the quartz-hosted melt inclusions was based on Al_2O_3, whose concentration was estimated from trends displayed by major and trace elements in whole-rock analyses, or was taken from microprobe analyses of exposed glassy inclusions. Because the Al_2O_3 concentration of whole-rocks varies relatively little within the interval 72–78 wt % SiO_2 the error introduced by this standardization procedure is less than 5% relative. Crystallized melt inclusions in slowly cooled samples have commonly lost a substantial portion of their original sodium concentration (e.g. Zajacz *et al.*, 2009). Thus, for crystallized melt inclusions we added Na numerically until the Na/K ratio was the same as that of the whole-rocks. This is, of course, only a crude approximation because the Na/K ratio of a whole-rock is not necessarily the same as that of a residual melt. The SiO_2 concentration of the melt inclusions was then calculated by difference assuming a total of 100 wt % major element oxides (volatile-free). In rapidly quenched samples a few exposed, glassy melt inclusions were analyzed without ablating the surrounding quartz. In this case, absolute concentrations were obtained by normalizing the sum of all major element oxides to 100 wt %.

RESULTS

Molybdenite inclusions in quartz phenocrysts occur as very thin (<1 μm) platelets with trigonal or hexagonal outline and sharp boundaries. Commonly the platelets are brownish and semi-transparent, and are oriented parallel to the quartz crystal surfaces (i.e. the platelets adhered to the walls of the growing crystals), with some having a small amount of melt attached on the face that pointed away from the growing quartz crystal (Fig. 1). The abundance of molybdenite inclusions in a given sample is highly variable (Table 1). Some samples contain molybdenite inclusions in every third or fourth quartz phenocryst (e.g. Huckleberry Ridge Tuff of Yellowstone, Pine Grove Tuff, Amalia Tuff), whereas other samples contain only one or two inclusions in ≥100 phenocrysts examined. It is thus possible that some of the samples listed here as

Table 1: Overview of samples studied

Magmatic system	Subunit	Age (Ma)	Tectonic setting
Molybdenite-saturated samples			
Atesina Volcanic Complex, Italy	Upper Group(?)	~275	within-plate
Caetano Caldera(?), NV	Caetano tuff(?); *NMNH 35327*	~34	?
Cave Peak, TX	Porphyritic quartz monzonite; *CP8*	~36·7	within-plate
Climax–Alma Batholith, CO	Treasure Mt. Dome, Bear Mt. facies	~12·4	within-plate
Coso Volcanic Field, CA	Dome 28 (group 2); *9-6-10*	0·59	within-plate
Coso Volcanic Field, CA	Dome 4 (group 7); *Coso 8*	0·06	within-plate
Jemez Mts. Volcanic Field, NM	Upper Bandelier tuff	~1·2	within-plate
Latir Volcanic Field, NM	Amalia Tuff	26	within-plate
Stronghold Granite, AZ	Late-stage rhyolite dike; Tr	22–28	within-plate
Thomas Range, UT	Topaz Mt. rhyolite; *NMNH 109593-10*	~6	within-plate
Toba Caldera, Indonesia	Toba Tuff; NMNH *116398-4*	0·074	volcanic arc
Wah Wah Mountains(?), UT	Southern end; *NMNH 35318*	~23	within-plate
Wah Wah Mountains, UT	Pine Grove tuff; air fall unit (Tbpa); *Pine 8*	22	within-plate
Wah Wah Mountains, UT	Pine Grove porphyry (Tpg); *Pine 2*	22	within-plate
Yellowstone, WY	Sulphur Creek tuff(?); *NMNH 28829*	0·48	within-plate
Yellowstone, WY	Huckleberry Ridge tuff	2·05	within-plate
?	*PCI*, *Y-TPI*	n.a.	?
Molybdenite-undersaturated(?) samples			
Alid Volcanic Center, Eritrea	Rhyolite pyroclastic flow	0·015	within-plate
Caetano Caldera(?), NV	Caetano tuff(?); *NMNH 35361*	~34	volcanic arc
Caliente Caldera(?), UT	Racer Canyon tuff(?)	18	within-plate
Capitan Pluton, NM	Granophyre facies; *Capi 3*	~27	within-plate
Cave Peak, TX	Late rhyolite dikes; *CP9*	~36·7	within-plate
Coso Volcanic Field, CA	Dome 38 (group 1); *8-197-4*	1·04	within-plate
Elkhorn Mts. Volcanics, MT	not known; *NMNH 116382-5*	77–79	volcanic arc
Kern Plateau, CA	Long Canyon dome	0·2	within-plate
Lassen Volcanic Center, CA	Sunflower Flat rhyodacite(?)	0·041	volcanic arc
Latir Volcanic Field, NM	Cañada Pinabete; biotite granite; *Cana 4*	~24·7	within-plate?
Latir Volcanic Field, NM	Questa Mine Series dikes; *Q3*, *Q4*, *86034*	24·3	within-plate?
Latir Volcanic Field, NM	Questa Bear Canyon intrusion	23·9	within-plate?
Long Valley Caldera, CA	Bishop tuff; *NMNH 116377-7*	0·73	within-plate
Long Valley Caldera, CA	Bishop tuff; *B72*	0·73	within-plate
Novarupta Caldera, Alaska	Katmai, 1912 eruption, *AK5*	0	volcanic arc
San Juan Volcanic Field, CO	Fish Canyon Tuff; *NMNH 116378-20*	27·6	volcanic arc
San Juan Volcanic Field, CO	Hinsdale Rhyolite; *NMNH 116378-34*	~22·4	within-plate
Santa Rita, NM	Rhyodacite and quartz monzodiorite dikes	~63	volcanic arc
Taupo Caldera, New Zealand	Taupo ignimbrite(?); *NMNH 116210-28*	<1	volcanic arc
Taupo Caldera, New Zealand	Taupo ignimbrite(?); *NMNH 116418-2*	<1	volcanic arc
Timber Mt. Caldera(?), NV	Rainier Mesa tuff(?); *NMNH 116383-5*	~11	within-plate
Tombstone, AZ	Rhyolite dike; Kri; *Lord2*	~76	volcanic arc
Turkey Creek Caldera, AZ	Rhyolite Canyon tuff; *NMNH 116376-11*	~26	?
Turkey Creek Caldera, AZ	not known	~26	?
Yellowstone, WY	Tuff of Bluff Point	0·16	within-plate
Yellowstone, WY	West Yellowstone flow	0·11	within-plate

(continued)

Table 1: Continued

Magmatic system	N_{qtz}^{exam}	N_{qtz}^{moly}	T_{zirc} (°C)	P (kbar)	log fO_2 (ΔNNO)	References
Molybdenite-saturated samples						
Atesina Volcanic Complex, Italy	140	7	814–821	n.a.	n.a.	1, 2
Caetano Caldera(?), NV	20	1	715–724	n.a.	n.a.	3, 4, 5
Cave Peak, TX	30	2	(936–1080)	1·2–1·5	n.a.	6, 7
Climax–Alma Batholith, CO	40	2	747–779	n.a.	n.a.	8, 9
Coso Volcanic Field, CA	300	2	(760–775)	2·7	−1·0	10, 11
Coso Volcanic Field, CA	300	2	(742–757)	1·4	−0·7	10, 11
Jemez Mts. Volcanic Field, NM	30	6	(809–832)	1·5–2·0	−0·7	12, 13, 14
Latir Volcanic Field, NM	40	10	814–821	0·8–1·4	(+1·5)	15, 16
Stronghold Granite, AZ	50	7	754–771	n.a.	n.a.	17, 18
Thomas Range, UT	20	4	776–803	n.a.	−0·7	19, 20, 21
Toba Caldera, Indonesia	100	2	726–742	3·0	+0·5	22, 23
Wah Wah Mountains(?), UT	30	2	701–715	n.a.	−0·7	21
Wah Wah Mountains, UT	50	12	707–724	4·3–2·5	(+0·8)	21, 24, 25
Wah Wah Mountains, UT	50	12	n.a.	4·3–2·5	(+0·8)	21, 24, 25
Yellowstone, WY	40	2	(792–825)	n.a.	−0·7	26, 27, 28
Yellowstone, WY	70	20	(774–805)	n.a.	−0·7	26, 27, 28
?	90	8	(822–849)	n.a.	n.a.	
Molybdenite-undersaturated(?) samples						
Alid Volcanic Center, Eritrea	60	none	(827–837)	0·4–0·9	NNO	29, 30, 31
Caetano Caldera(?), NV	50	none	726–736	n.a.	n.a.	3, 4
Caliente Caldera(?), UT	70	none	723–739	n.a.	n.a.	32, 33
Capitan Pluton, NM	90	none	845–875	<1·0	n.a.	34, 35
Cave Peak, TX	20	none	(966–1034)	1·2–1·5	n.a.	6, 7
Coso Volcanic Field, CA	400	none	747–754	n.a.	n.a.	10
Elkhorn Mts. Volcanics, MT	30	none	712–728	n.a.	n.a.	36, 37
Kern Plateau, CA	300	none	(711–728)	n.a.	+0·2	38
Lassen Volcanic Center, CA	120	none	712–723	n.a.	n.a.	39, 40
Latir Volcanic Field, NM	70	none	738–771	1·2–1·3	(+1·5)	41, 42
Latir Volcanic Field, NM	170	none	710–760	<1·0	(+1·5)	43
Latir Volcanic Field, NM	20	none	744	<1·0	(+1·5)	41
Long Valley Caldera, CA	20	none	727–731	1·5–2·1	+0·1	5, 44
Long Valley Caldera, CA	70	none	737–750	1·5–2·1	+0·1	5, 44
Novarupta Caldera, Alaska	80	none	775–788	>1·0	NNO	45, 46
San Juan Volcanic Field, CO	10	none	724–727	2·2–2·5	+1·3	47, 48, 49
San Juan Volcanic Field, CO	30	none	797–806	n.a.	n.a.	50, 51, 52
Santa Rita, NM	30	none	710–739	1·0–3·0	+1·5	53, 54, 55
Taupo Caldera, New Zealand	30	none	727–763	1·6–2·0	+0·3	56, 57, 58, 59
Taupo Caldera, New Zealand	30	none	726–771	1·6–2·0	+0·3	56, 57, 58, 59
Timber Mt. Caldera(?), NV	20	none	706–722	3·9–4·5	+1·6	60
Tombstone, AZ	20	none	669–680	n.a.	n.a.	61, 62
Turkey Creek Caldera, AZ	10	none	848–853	n.a.	n.a.	63, 64
Turkey Creek Caldera, AZ	300	none	857–874	n.a.	n.a.	63, 64
Yellowstone, WY	100	none	(791–815)	n.a.	−1·5	26, 27
Yellowstone, WY	300	none	(809–824)	n.a.	−1·5	26, 27

?, unknown or uncertain. Sample names are shown in italics; samples from the Smithsonian Institution start with NMNH. Tectonic setting is as suggested by previous workers. N_{qtz}^{exam}, approximate number of quartz phenocrysts examined. N_{qtz}^{moly}, number of quartz phenocrysts with molybdenite inclusions. T_{zirc}, zircon saturation temperatures calculated from the range of Zr concentrations measured in melt inclusions; values in parentheses are for peralkaline melts and thus represent maximum values. Typical uncertainty for log fO_2 is ±0·3 log units; estimates with higher uncertainty are shown in parantheses. References are given in Electronic Appendix I. n.a., not available.

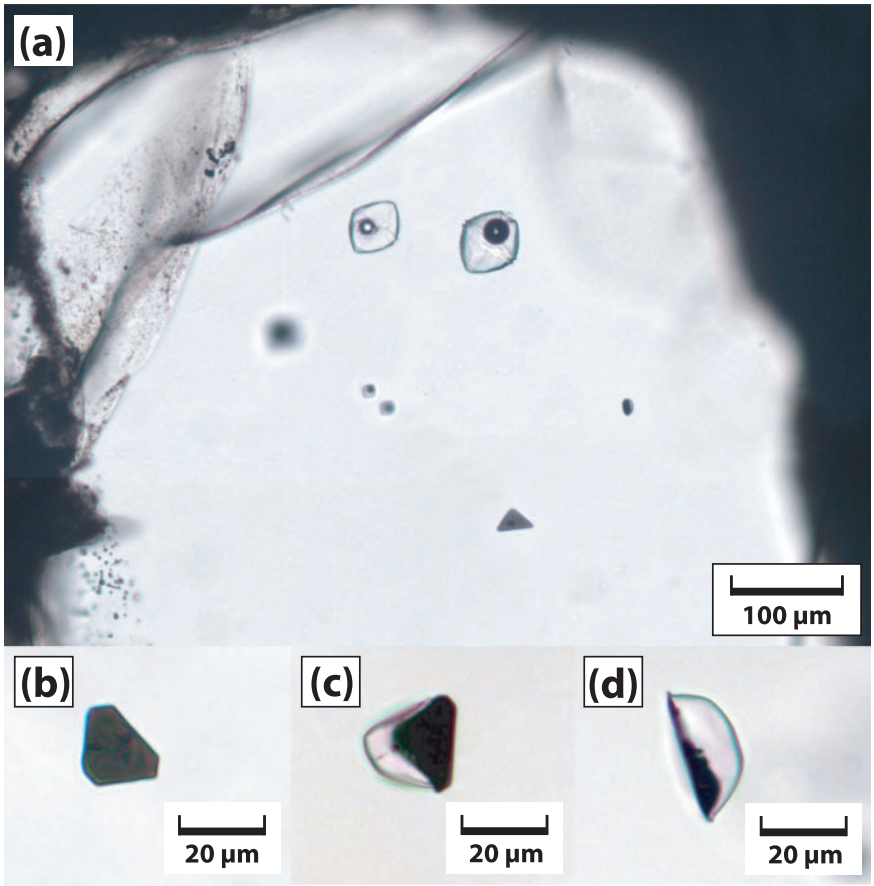

Fig. 1. Examples of magmatic molybdenite inclusions in quartz phenocrysts from high-silica rhyolite tuffs. (a) Triangular, semi-transparent crystal and coexisting melt inclusions from the Amalia Tuff, Latir volcanic field, New Mexico. (b) Semi-transparent crystal from the Pine Grove Tuff, Wah Wah Mountains, Utah. (c, d) Molybdenite crystals with attached melt droplets from the Upper Bandelier Tuff, Jemez Volcanic field, New Mexico. All photographs taken in transmitted light.

molybdenite-undersaturated could be molybdenite-saturated if rare inclusions were missed.

Analyzed melt inclusions are mostly high-silica rhyolites (>75 wt % SiO_2), with molar $Al_2O_3/(Na_2O+K_2O)$ ranging from 0·90 (peralkaline) to 1·20, and molar $Al_2O_3/(CaO+Na_2O+K_2O)$ ranging from 0·85 to 1·20 (peraluminous) if only glassy inclusions are considered, because crystallized melt inclusions typically have lost Na. All melt inclusions contain high concentrations of incompatible elements such as Rb and Cs (up to 1000 ppm and 60 ppm, respectively), and low concentrations of compatible elements such as Sr and Ba (down to <1 ppm each). The full analytical dataset is given in Electronic Appendix II. Molybdenum concentrations are 1–13 ppm in molybdenite-saturated samples and 1–17 ppm Mo in molybdenite-undersaturated samples, with no apparent correlation between the presence of molybdenite and the degree of melt fractionation as implied by Rb (or Mo) concentration (Fig. 2). Variations in Mo concentrations in single samples are typically small (less than 50% relative; Electronic Appendix II), and in some cases correlate sympathetically with other trace elements, implying that these variations are real and not an analytical artefact.

Trace element signatures of melt inclusions from molybdenite-saturated samples show a clear affinity to within-plate granites and, thus dominantly, to an enriched mantle source (Pearce *et al.*, 1984), whereas those of melt inclusions from molybdenite-undersaturated samples are more diverse and cover the fields of within-plate, volcanic arc, and syn-collisional granites (Fig. 3). This geochemical interpretation fits well with the tectonic settings inferred for the investigated magma suites based on age and structural relationships, as shown in Table 1. All molybdenite-bearing samples come from igneous suites within plate interiors, except for the Toba Tuff, which formed in a subduction setting with an apparent transtensional component. Furthermore, all four magma suites that are genetically related to porphyry Mo mineralization are saturated in molybdenite. This is consistent with the interpretation by Carten *et al.* (1993) that these ore deposits

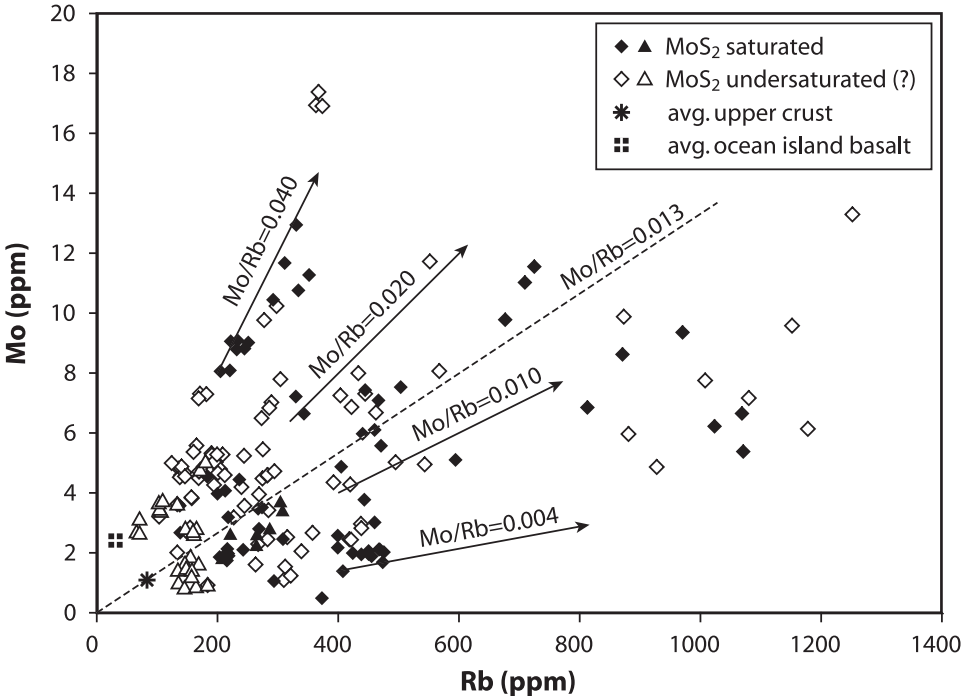

Fig. 2. Molybdenum and Rb concentrations in the analyzed melt inclusions, plotted together with the average compositions of upper continental crust (Rudnick & Gao, 2003) and ocean-island basalts (Sun & McDonough, 1989), and fractionation trends followed during closed-system fractional crystallization of melts with various Mo/Rb ratios if Mo and Rb were similarly incompatible in the crystallizing minerals. Diamonds denote melts from within-plate settings; triangles denote melts from volcanic arc settings.

(Pine Grove, Cave Peak, Questa/Latir Volcanic Field and Climax–Henderson/Treasure Mt. Dome) and their host magmatic suites are related to continental extension.

Investigated samples from typical subduction-related magmas seem to be all molybdenite-undersaturated, containing <200 ppm Rb and 1–5 ppm Mo (average 2·3 ppm). At these Mo concentrations, several within-plate magma systems (Atesina volcanic complex, Coso volcanic field and Pine Grove) have already reached molybdenite saturation (Fig. 2). The apparent lack of molybdenite saturation in subduction-related magmas may be a consequence of their more oxidized character and associated higher MoS_2 solubility, as discussed below.

DISCUSSION

Source of molybdenum

The source of molybdenum in mineralized magmatic suites has been controversial. For Mo-rich provinces such as the Colorado Mineral Belt, which has been the locus of repeated Mo-mineralization over a time span of more than one billion years, it has been suggested that molybdenum originated locally from the upper crust (e.g. Sinclair, 2007; Zhu *et al.*, 2009). Westra & Keith (1981), Keith *et al.* (1986) and Carten *et al.* (1993), on the other hand, advocated a mantle origin for the molybdenum owing to the strong link of porphyry molybdenum mineralizing magmas to within-plate basalts. A direct derivation of Mo from mafic, rift-related magmas through fractional crystallization has recently been suggested for the mineralizing magmas at Cave Peak (Audétat, 2010). In agreement with this scenario, our melt inclusion data support a deep origin of molybdenum. Many of the analyzed melt inclusions have Mo/Rb ratios distinctly higher than that of average upper and middle continental crust (Mo/Rb = 0·013 and 0·009, respectively; Rudnick & Gao, 2003; Mo/Rb of average upper continental crust shown by the dashed line in Fig. 2). Such melts are unlikely to have evolved from average upper or middle crust because the high incompatibility of Rb requires that Mo/Rb can only be lowered (but not increased) during partial melting or fractional crystallization. Melts with Mo/Rb much higher than 0·013 need to be derived from sources that include a component with higher Mo/Rb, such as average lower continental crust (Mo/Rb = 0·055; Rudnick & Gao, 2003) or mafic alkaline magmas produced by low-degree partial melting of metasomatized mantle; that is, continental rift basalts or ocean island basalts (average Mo/Rb = 0·077; Sun & McDonough, 1989).

Crystallization conditions

To explore the mechanisms for molybdenite saturation in rhyolitic magmas it is important to estimate the magmatic conditions that would control phase equilibria. Estimated

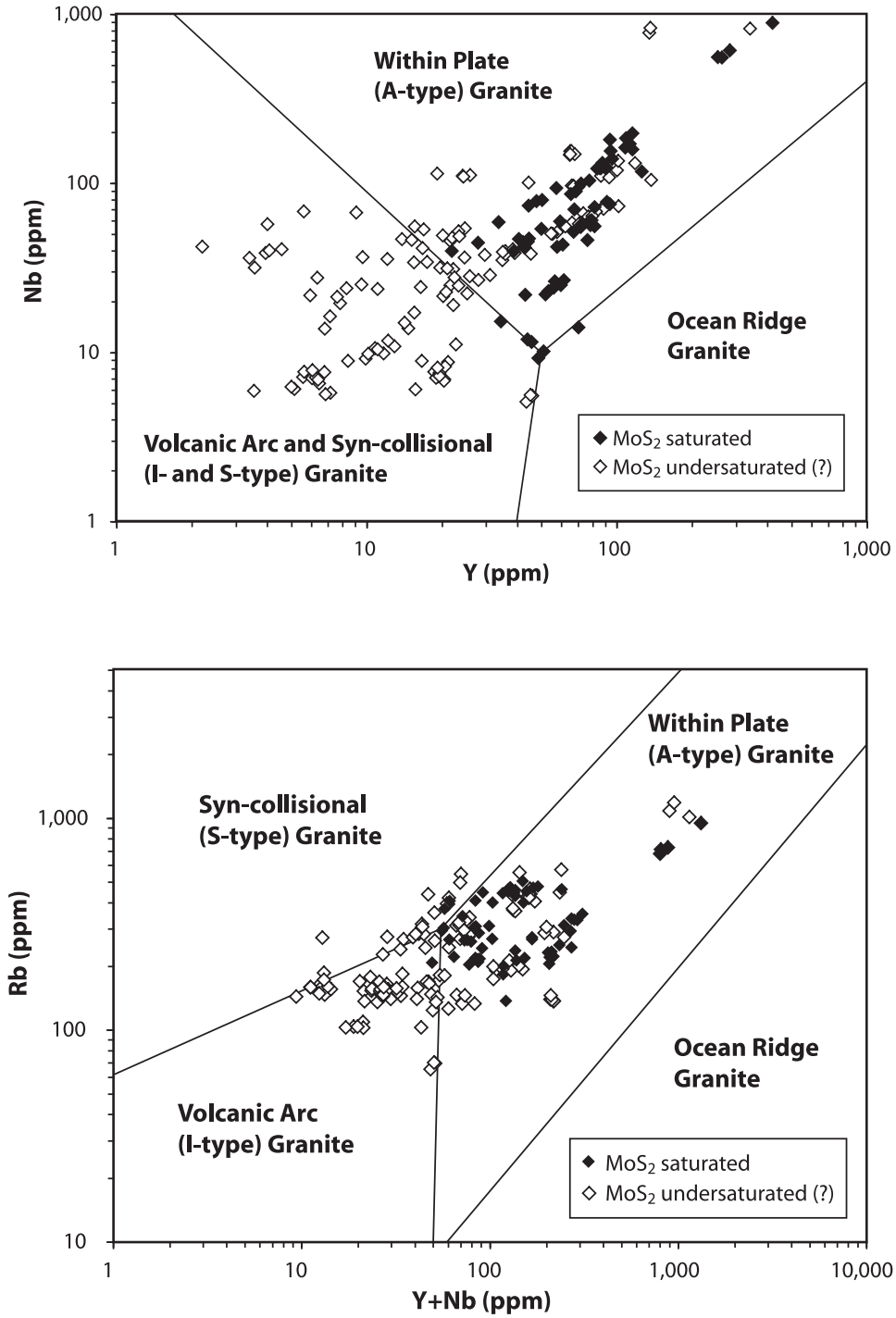

Fig. 3. Geochemical interpretation of the analyzed melt inclusions according to tectonic discrimination diagrams of Pearce *et al.* (1984). Molybdenite-saturated melts show a strong affinity to within-plate (or A-type) granites, whereas molybdenite-undersaturated melts plot in all fields except for ocean-ridge granites.

crystallization conditions of MoS_2-saturated magmas are shown in Fig. 4, together with the measured Mo concentrations in melt inclusions. Temperature estimates represent zircon saturation temperatures calculated based on the Zr content of the melt inclusions (Electronic Appendix II). The common presence of zircon inclusions within our studied quartz phenocrysts suggests that most (if not all) of our analyzed melt inclusions were saturated in zircon.

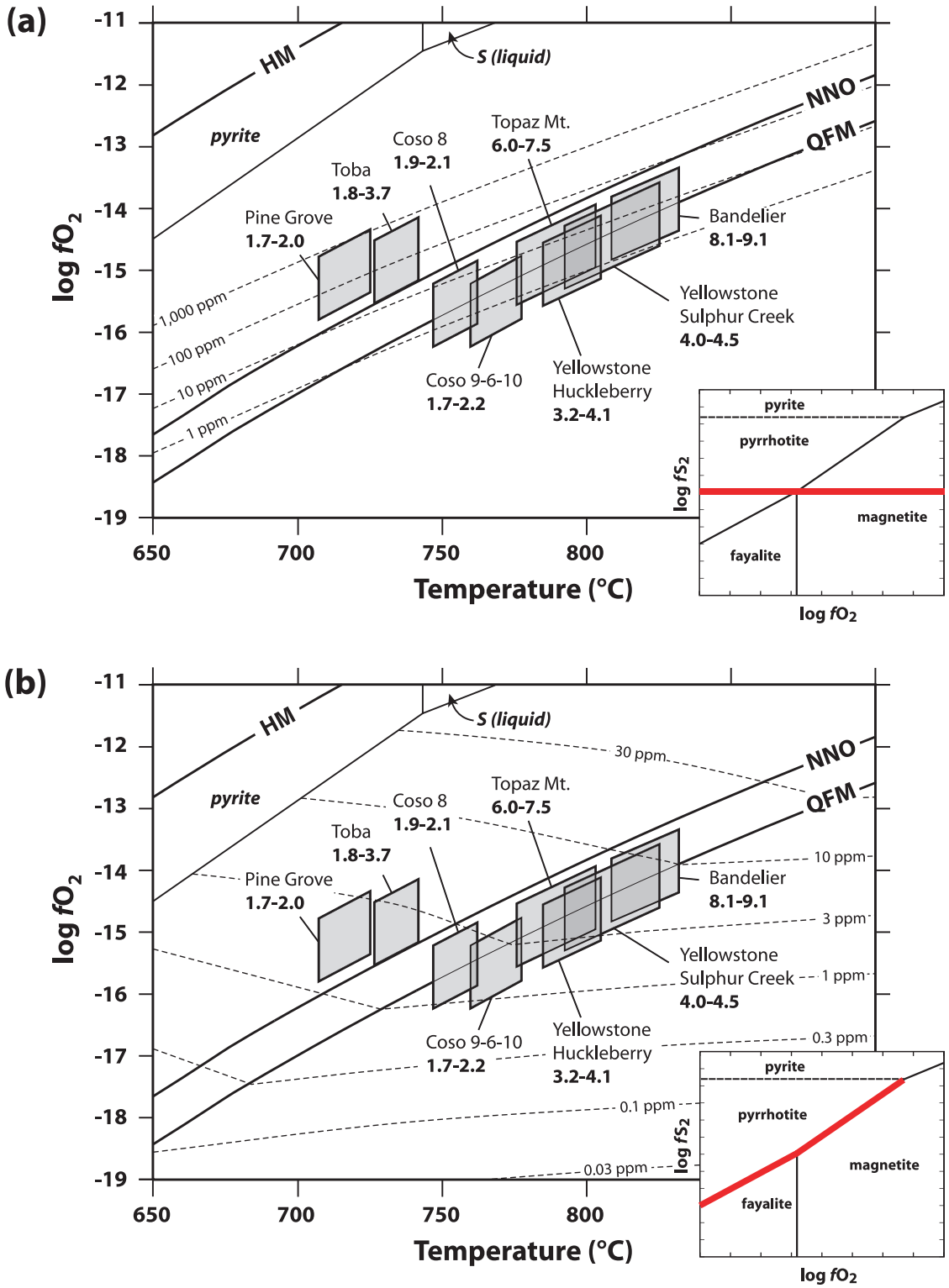

Fig. 4. Estimated T–fO_2 entrapment conditions and analyzed Mo contents of molybdenite-saturated samples, in comparison with thermodynamically predicted MoS_2 solubilities and phase relations. Values in bold beneath the sample names indicate the range of measured Mo concentrations in ppm. HM, hematite–magnetite; NNO, nickel–nickel oxide; QFM, quartz–fayalite–magnetite. Thermodynamic predictions of MoS_2 solubilities were made for two fS_2 scenarios, as shown schematically in the insets: (a) fS_2 is fixed at the value corresponding to the assemblage pyrrhotite–magnetite–fayalite; (b) fS_2 is buffered by the assemblage pyrrhotite–magnetite or pyrrhotite–fayalite, which constrains fS_2 as a function of fO_2. The stability fields of pyrite and sulfur liquid apply to a condensed system.

The Zr concentration of melts provides a much more rigorous estimate of trapping temperature than whole-rock Zr contents because the latter can be enriched by accumulation of Zr-rich crystals or be diluted by accumulation of other phenocryst phases. For calculating zircon saturation temperatures we have used the formulation of Watson & Harrison (1983); however, it should be noted that this thermometer was calibrated only for metaluminous and peraluminous melts and tends to overestimate true temperatures if applied to peralkaline melts. For this reason, temperatures for peralkaline compositions shown in parentheses in Table 1 should be regarded only as maximum values. Our calculated temperatures for metaluminous and peraluminous melts are in good agreement with literature data based on magnetite–ilmenite pairs, although the latter commonly give a significantly larger range. Oxygen fugacity (fO_2) values shown in Fig. 4 represent literature values derived from magnetite–ilmenite pairs and include an implicit uncertainty of ±0·5 log units. Most data points cluster around the quartz–fayalite–magnetite (QFM) buffer, which is consistent with the presence of fayalite ($Fa_{86–94}$) in the studied magmas from the Coso Volcanic field, the Yellowstone Caldera, and the Bandelier Tuff (Warshaw & Smith, 1988; Manley & Bacon, 2000; Vazquez *et al.*, 2009). It should be noted that dissolved Mo concentrations in samples plotting along the QFM buffer increase with increasing temperature.

Thermodynamic modeling

To explore the separate effects of temperature, fO_2 and fS_2 on molybdenite solubility, we formulated a simple thermodynamic model based on available information on Mo speciation in silicate melts. At the fO_2 conditions of our samples, Mo is dissolved dominantly in the form of molybdate; that is, $Mo(VI)O_4^{2-}$ (Farges *et al.*, 2006*a*, 2006*b*). The thermodynamic species corresponding to molybdate is liquid MoO_3, thus molybdenite solubility can be described as follows (Lowenstern *et al.*, 1993):

$$2\ MoO_3\ (melt) + 2\ S_2\ (system) = 2\ MoS_2\ (molybdenite) + 3\ O_2\ (system). \quad (1)$$

According to this reaction the Mo concentration of MoS_2-saturated melts should increase with increasing fO_2 or decreasing fS_2. The Mo concentration should also increase with increasing temperature (Isuk & Carman, 1981), and potentially it could depend on melt composition, although the local environment of Mo has not been observed to change as a function of melt polymerization or halogen (Cl, F) content (Farges *et al.*, 2006*a*, 2006*b*). We have calculated the Mo concentration of MoS_2-saturated melts at any given temperature for two scenarios: (1) fS_2 is fixed at the value corresponding to the assemblage pyrrhotite–magnetite–fayalite; (2) fS_2 buffered by the assemblage pyrrhotite–magnetite or pyrrhotite–fayalite, which constrains fS_2 as a function of fO_2 (e.g. Whitney, 1984). The reactions corresponding to the latter buffering scenario are

$$2\ Fe_3O_4\ (magnetite) + 3\ S_2\ (g) = 6\ FeS\ (pyrrhotite) + 4\ O_2\ (g) \quad (2)$$

$$Fe_2SiO_4(fayalite) + S_2(g) = 2\ FeS\ (pyrrhotite) + SiO_2 + O_2(g). \quad (3)$$

Equations (1) and (2) apply to magmas above the QFM buffer whereas equations (1) and (3) are used at more reducing conditions. To calculate these equilibria we used standard state thermodynamic data from the following sources: Robie & Hemingway (1995) for sulfur, Holland & Powell (1998) for fayalite and oxides, Chase (1998) for molybdenum compounds, and Waldner & Pelton (2005) for iron sulfides. These data define standard Gibbs energies (in Joules) at 1 bar of equilibria in equations (1)–(3) using ideal gas standard state for O_2 and S_2, respectively, as follows:

$$\Delta_{r(1)}G^\circ = 321269 - 276 \cdot 509\ T + 33 \cdot 298\ T\ \ln\ T \quad (4)$$

$$\Delta_{r(2)}G^\circ = 1278395 - 461 \cdot 598\ T + 25 \cdot 530\ T\ \ln\ T \quad (5)$$

$$\Delta_{r(3)}G^\circ = 263879 - 70 \cdot 110\ T + 4 \cdot 730\ T\ \ln\ T \quad (6)$$

where T is temperature in Kelvin. Pyrrhotite, $Fe_{1-x}S$, is non-stoichiometric because its cation site is partly vacant (Fleet, 1971). It was treated as a non-ideal solid solution between an iron-bearing end-member (FeS) and a vacancy-bearing end-member (□S), with high-temperature hexagonal crystal structures (Waldner & Pelton, 2005). The standard Gibbs energy of formation of the hypothetical hexagonal end-member □S from gaseous diatomic sulfur,

$$1/2\ S_2\ (g) \rightarrow \square S\ (pyrrhotite) \quad (7)$$

is equal to (Waldner & Pelton, 2005)

$$\Delta_rG^\circ = 70167 + 170 \cdot 702\ T - 12 \cdot 662\ T\ \ln\ T. \quad (8)$$

The excess mixing energy between the FeS and □S end-members with the pyrrhotite structure was described by a symmetric Margules parameter (Waldner & Pelton, 2005):

$$W = -225831 + 26 \cdot 359\ T. \quad (9)$$

As a first approximation, the liquid MoO_3 species was assumed to mix with the quasicrystalline silicate melt species on an eight-oxygen basis ideally (Burnham, 1997). The Henrian activity coefficient of MoO_3 in the melt, γMoO_3, was later adjusted to 1·25 ± 0·19 to provide a slightly better fit to the data (see below). To convert the calculated mole fraction of MoO_3 in the melt to its molybdenum concentration by mass (in ppm), the molar mass

of the melt on an eight-oxygen basis is required. We have used the value of 258 g mol^{-1}, which corresponds to a haplogranitic minimum composition at 1 kbar (Tuttle & Bowen, 1958); no other information about the melt composition is necessary.

For each sample, the thermodynamic calculation of the molybdenum solubility consisted of the following steps.

(1) Calculation of pyrrhotite composition and sulfur fugacity by solving the mass action law; that is, equilibrium constant expressions for equilibria (2) or (3) and (7) simultaneously. The use of equation (2) or (3) is dictated by the location of the sample above or below the QFM buffer, respectively. Because the activity coefficients for pyrrhotite end-members are composition-dependent, the solution was found iteratively.
(2) Calculation of the MoO_3 concentration in the melt by using the mass action law for equation (1) at the sulfur fugacity obtained in the previous step.

The results are illustrated in Fig. 4. In both the scenario of fS_2 fixed at the value corresponding to the assemblage pyrrhotite–magnetite–fayalite (Fig. 4a) and fS_2 buffered by the assemblages pyrrhotite–magnetite or pyrrhotite–fayalite (Fig. 4b), molybdenite solubility increases with increasing temperature along the shown redox buffers. However, if fS_2 fixed at the value of the pyrrhotite–magnetite–fayalite invariant point (corresponding to a pyrrhotite composition of $a_{FeS}^{po} = 0{\cdot}85$) molybdenite solubility should increase by nearly two orders of magnitude over the range of T–fO_2 conditions covered by our data, which is in strong contrast to the observed range of ~2–9 ppm Mo in the analyzed melt inclusions. Our second scenario with fS_2 buffered by the assemblage pyrrhotite–magnetite or pyrrhotite–fayalite predicts a more moderate increase in MoS_2 solubility with increasing fO_2 and thus provides a much better fit to our data (Fig. 4b). Minor deviations may be due to (1) inaccuracies in T and fO_2 estimates, (2) lack of actual pyrrhotite saturation, or (3) variations in γMoO_3. If MoO_3 is assumed to mix ideally ($\gamma MoO_3 = 1{\cdot}0$) the thermodynamic model reproduces our data with an actual deviation of 1·26 ppm without any additional assumptions. The accuracy can be further improved by introducing an activity coefficient of $\gamma MoO_3 = 1{\cdot}25$, resulting in reproduction of our data to within 0·70 ppm. This activity coefficient has thus been used for the calculations of molybdenum solubility isopleths in Fig. 4. Neglecting γMoO_3 would shift the isopleths in Fig. 4 marginally downwards (by about 0·1 log unit).

Pyrrhotite saturation

Of the six magma suites plotted in Fig. 4, pyrrhotite has been reported only from the Toba Tuff (Chesner, 1998) and from the Yellowstone rhyolites (Gardner, 2007). However, considering the evolved character of our samples (with only little Fe being available to produce pyrrhotite), combined with the fact that magmatic sulfides rapidly oxidize at subsolidus conditions (e.g. Whitney, 1984; Stavast *et al.*, 2006), it is not unlikely that pyrrhotite was in fact present in most or all. If preserved only as inclusions in phenocrysts, pyrrhotite is difficult to identify if it is not accidentally exposed by polishing, because it lacks a characteristic appearance such as molybdenite platelets and is only weakly Raman active, thus looking identical to the much more abundant magnetite inclusions. The fS_2–fO_2 plots in Fig. 5 suggest that all the magmas shown in Fig. 4 were at or very close to pyrrhotite saturation. Taking the 800°C isotherm as an example (Fig. 5a) it can be seen that at fO_2 and fS_2 conditions defined by the coexistence of pyrrhotite, magnetite and fayalite the observed molybdenite solubilities of 3·2–4·5 ppm Mo in the Yellowstone samples and 6·0–7·5 ppm Mo in the Topaz Mt. rhyolite fit very well between the 1 ppm and 10 ppm isopleths of our solubility model. Whereas magnetite and fayalite occur in both the Yellowstone samples and the Topaz Mt. rhyolite, pyrrhotite has so far been reported only from Yellowstone. However, owing to the narrow spacing of the solubility isopleths it is evident that if fS_2 were only 0·5 log unit below pyrrhotite–magnetite–fayalite triple point, then the molybdenite solubility would have exceeded 10 ppm and thus would be incompatible with the observed range of 6·0–7·5 ppm. The same reasoning can be used to demonstrate that fS_2 must have been within 0·5 log units of pyrrhotite saturation also at Pine Grove (Fig. 5b), as well as in all other samples plotted in Fig. 4 (fS_2–fO_2 sections at the corresponding temperatures are not shown). In pyrrhotite-undersaturated magmas, fS_2 would be reduced, and hence MoS_2 solubility would be higher than indicated by the isopleths in Fig. 4. We provide an Excel spreadsheet to calculate molybdenite solubility in pyrrhotite-bearing magmas saturated in quartz + magnetite (or fayalite) at known temperature and fO_2 (Electronic Appendix III). This spreadsheet can inversely be used to estimate fO_2 and fS_2 in molybdenite-saturated magmas if temperature and the Mo concentration in the melt are known.

Implications for magma evolution

Molybdenite (60 wt % Mo) contains about 100 000 times more Mo than the coexisting melt. Once molybdenite saturation has been attained the Mo concentration of the melt is capped and cannot increase unless conditions of higher MoS_2 solubility are induced by changes in temperature, fO_2 or fS_2. Magmatic molybdenite saturation could thus be the reason why silicate melts rarely contain more than 20 ppm Mo, even in highly fractionated pegmatitic liquids (Zajacz *et al.*, 2008). Other potential factors limiting Mo enrichment in residual melts are Mo removal by exsolving fluids (e.g. Candela & Holland, 1984; Keppler & Wyllie, 1991; Webster, 1997; Audétat *et al.*, 2008; Zajacz

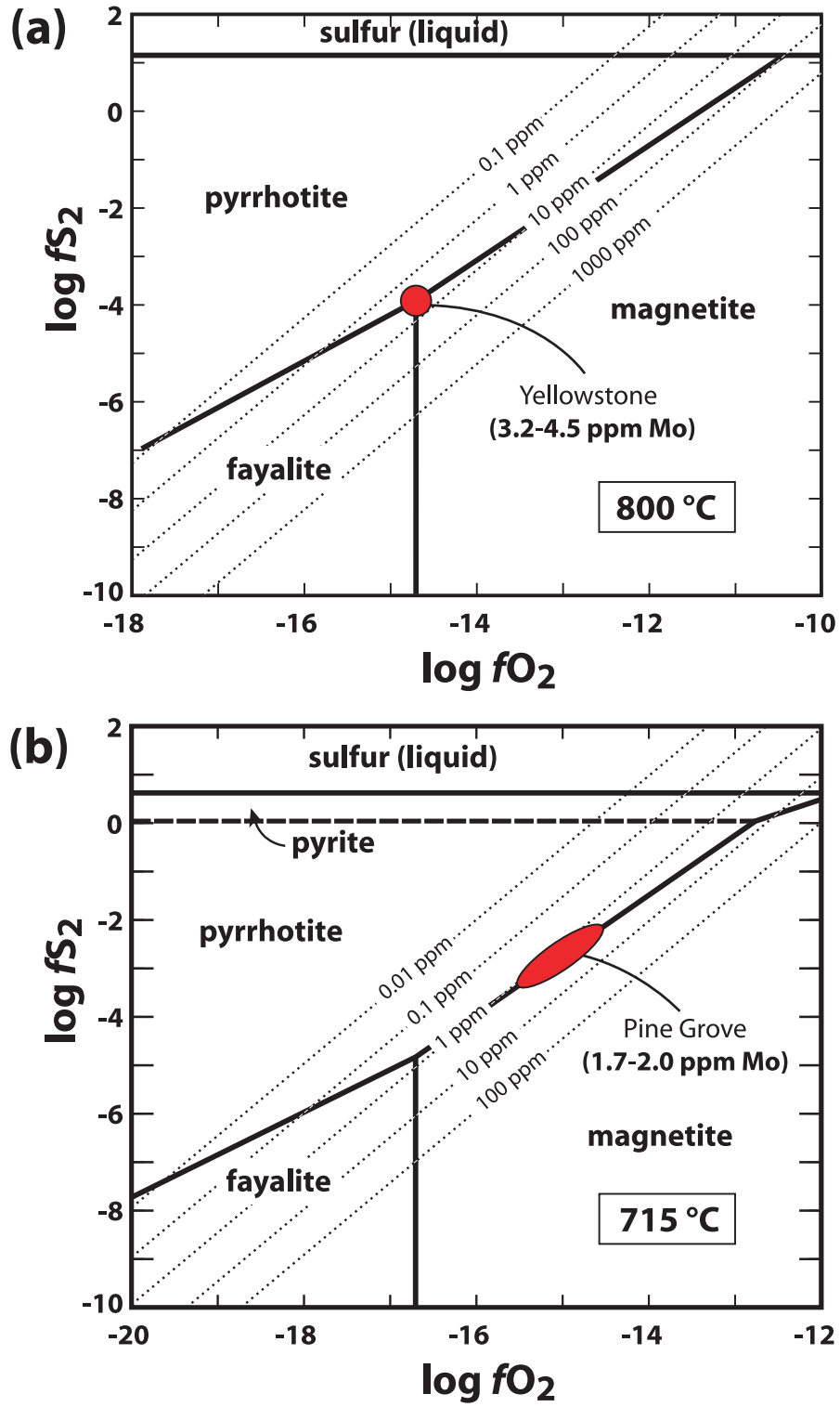

Fig. 5. Isothermal fS_2 vs fO_2 plots showing calculated MoS_2 solubilites at temperatures relevant for several of the occurrences shown in Fig. 4. (a) The Huckleberry Ridge and Sulphur Creek rhyolites from Yellowstone plus the Topaz Mt. rhyolite (all *c.* 800°C), and (b) the Pine Grove tuff (*c.* 715°C). Measured molybdenum concentrations in the melt inclusions are in excellent agreement with predicted MoS_2 solubilities if the magmas are assumed to have also been saturated in pyrrhotite (shaded circle or ellipse), but would be significantly underestimated if fS_2 was ≥0·5 log units below the pyrrhotite stability field. Solid phase boundaries refer to $P=1$ bar but show negligible pressure dependence, ~0·1 log unit per kbar.

et al., 2008; Audétat, 2010) or Mo incorporation into crystallizing minerals such as magnetite, ilmenite or pyrrhotite, although the corresponding crystal/melt partition coefficients and absolute mineral abundances seem to be too small to allow a dominant control on the Mo budget of the residual melt (Tacker & Candela, 1987; Stimac & Hickmott, 1994; Audétat, 2010).

Another consequence of magmatic molybdenite saturation is that Mo can be fractionated by physical processes. Gravitational settling is probably not very efficient because of the small size of the MoS_2 crystals and their tendency to adhere to (quartz) phenocrysts. On the other hand, it may be feasible that Mo is transported upward by means of MoS_2 platelets attached to rising fluid bubbles. Given that MoS_2 is naturally hydrophobic and thus easy to float, such a process would render models of Mo transport via magmatic fluids (e.g. Shinohara *et al.*, 1995) even more effective. We emphasize that our observation of magmatic molybdenite saturation in all four samples that are related to porphyry Mo probably reflects the genetic association of these rhyolites with within-plate magmas and does not provide evidence that magmatic crystallization of molybdenite is a prerequisite to produce economic molybdenum mineralization. In fact, our data confirm earlier findings that the Mo concentrations of rhyolitic liquids associated with mineralization are extremely low and that metal enrichment by magmatic–hydrothermal fluids remains the key mechanism to form Mo mineralization. Furthermore, more than half of the world's molybdenum production stems from porphyry Cu–Mo deposits (McCready, 2007), which are associated with subduction-related magmas that show no evidence for molybdenite saturation; from our sample set, the Cu–Mo–Au porphyry at Santa Rita is a representative example (see Audétat & Pettke, 2006).

CONCLUSIONS

We have demonstrated that molybdenite is a relatively common accessory phase in silicic magmas. Magmatic molybdenite saturation is more frequent in within-plate rhyolitic magmas, probably because they are more reduced than their arc counterparts (e.g. Herd, 2008; Jugo *et al.*, 2010).

The excellent agreement between measured Mo concentrations and thermodynamically predicted MoS_2 solubilities at pyrrhotite saturation suggests that most of our molybdenite-saturated samples were at or very close to pyrrhotite saturation. In such magmas the Mo content of the melt can be used to estimate magmatic fO_2 and fS_2 if temperature is known (e.g. from zircon saturation thermometry; Watson & Harrison, 1983). In magmas containing molybdenite but where there is uncertainty whether or not they have been pyrrhotite-saturated, the Mo concentration of the melt can still be used to calculate fS_2 if temperature and fO_2 can be estimated independently (e.g. by Fe–Ti-oxide thermobarometry; Frost & Lindsley, 1992; Ghiorso & Evans, 2008). Sulfur fugacity is a crucial parameter that remains very difficult to estimate in natural magmas and rocks. Previous approaches using pyrrhotite composition (Whitney, 1984) or sulfur content in the melt (Clemente *et al.*, 2004) require rapidly quenched samples and are thus restricted to certain volcanic settings. Our approach, which utilizes petrographic recognition of molybdenite saturation and the Mo concentrations in coeval melt inclusions, provides a way to constrain fO_2 and fS_2 also in slowly cooled plutonic and volcanic rocks.

ACKNOWLEDGEMENTS

We thank Sorena Sorensen, Leslie Hale (both at the Smithsonian Institution) and Charles Bacon (USGS) for providing samples of quartz-bearing rhyolites, and Hubert Schulze and Uwe Dittmann (Bayerisches Geoinstitut) for the preparation of polished sections. Tom Sisson, David John, Bruno Scaillet and Jim Webster provided excellent comments on earlier versions of this paper, and we are indebted to John Dilles, Dima Kamenetsky and Zoltan Zajacz for their thorough and constructive reviews.

FUNDING

This study was supported by the Ministry of Education of the Czech Republic Research Plan (MSM 0021620855 to D.D.) and the Czech Science Foundation (Project 205/09/P135 to D.D.)

SUPPLEMENTARY DATA

Supplementary data for this paper are available at *Journal of Petrology* online.

REFERENCES

Audétat, A. (2010). Source and evolution of molybdenum in the porphyry Mo(–Nb) deposit at Cave Peak, Texas. *Journal of Petrology* **51**, 1739–1760.

Audétat, A. & Pettke, T. (2006). Evolution of a porphyry-Cu mineralized magma system at Santa Rita, New Mexico (USA). *Journal of Petrology* **47**, 2021–2046.

Audétat, A., Pettke, T., Heinrich, C. A. & Bodnar, R. J. (2008). The composition of magmatic–hydrothermal fluids in barren and mineralized intrusions. *Economic Geology* **103**, 877–908.

Briffa, K. R., Jones, P. D., Schweingruber, F. H. & Osborn, T. J. (1998). Influence of volcanic eruptions on Northern Hemisphere summer temperature over the past 600 years. *Nature* **393**, 450–454.

Burnham, C. W. (1997). Magmas and hydrothermal fluids. In: Barnes, H. L. (ed.) *Geochemistry of Hydrothermal Ore Deposits*, 3rd edn. New York: John Wiley, pp. 63–124.

Candela, P. A. & Holland, H. D. (1984). The partitioning of copper and molybdenum between silicate melts and aqueous fluids. *Geochimica et Cosmochimica Acta* **48**, 373–388.

Carroll, M. R. & Webster, J. D. (1994). Solubilities of sulfur, noble gases, nitrogen, chlorine, and fluorine in magmas. In: Carroll, M. R. & Holloway, J. R. (eds) *Volatiles in Magmas. Mineralogical Society of America, Reviews in Mineralogy* **30**, 251–279.

Carten, R. B., White, W. H. & Stein, H. J. (1993). High-grade granite-related molybdenum systems: Classification and origin. In: Kirkham, R. V., Sinclair, W. D., Thorpe, R. I. & Duke, J. M. (eds) *Mineral Deposit Modeling. Geological Association of Canada, Special Papers* **40**, 521–554.

Chase, M. W. (1998). *NIST JANAF Thermochemical Tables (4th edition). American Chemical Society, Journal of Physical and Chemical Reference Data, Monograph* **9**, 1951 p.

Chesner, C. A. (1998). Petrogenesis of the Toba Tuffs, Sumatra, Indonesia. *Journal of Petrology* **39**, 397–438.

Clemente, B., Scaillet, B. & Pichavant, M. (2004). The solubility of sulphur in hydrous rhyolitic melts. *Journal of Petrology* **45**, 2171–2196.

Farges, F., Siewert, R., Brown, G. E., Guesdon, A. & Morin, G. (2006*a*). Structural environments around molybdenum in silicate glasses and melts. I. Influence of composition and oxygen fugacity on the local structure of molybdenum. *Canadian Mineralogist* **44**, 731–753.

Farges, F., Siewert, R., Ponader, C. W., Brown, G. E., Pichavant, M. & Behrens, H. (2006*b*). Structural environments around molybdenum in silicate glasses and melts. II. Effect of temperature, pressure, H_2O, halogens and sulfur. *Canadian Mineralogist* **44**, 755–773.

Fleet, M. E. (1971). The crystal structure of a pyrrhotite (Fe_7S_8). *Acta Crystallographica* **B27**, 1864–1867.

Frost, B. R. & Lindsley, D. H. (1992). Equilibria among Fe–Ti-oxides, pyroxenes, olivine, and quartz: Part I. Theory. *American Mineralogist* **77**, 987–1003.

Gardner, J. E. (2007). Storage of explosive versus effusive rhyolite magma at the Yellowstone Volcanic Center. *American Geophysical Union, Fall Meeting* , Abstract No. V53B-1323.

Ghiorso, M. S. & Evans, B. W. (2008). Thermodynamics of rhombohedral oxide solid solutions and a revision of the Fe–Ti two-oxide geothermometer and oxygen-barometer. *American Journal of Science* **308**, 957–1039.

Günther, D., Audétat, A., Frischknecht, R. & Heinrich, C. A. (1998). Quantitative analysis of major, minor and trace elements in fluid inclusions using laser ablation-inductively coupled plasma-mass spectrometry (LA-ICP-MS). *Journal of Analytical Atomic Spectrometry* **13**, 263–270.

Halter, W. E., Pettke, T., Heinrich, C. A. & Roth-Rutishauser, B. (2002). Major to trace element analysis of melt inclusions by laser-ablation ICP-MS: methods of quantification. *Chemical Geology* **183**, 63–86.

Hedenquist, J. W. & Lowenstern, J. B. (1994). The role of magmas in the formation of hydrothermal ore deposits. *Nature* **370**, 519–527.

Heinrich, C. A., Pettke, T., Halter, W., Aigner-Torres, M., Audétat, A., Günther, D., Hattendorf, B., Bleiner, D., Guillong, M. & Horn, I. (2003). Quantitative multi-element analysis of minerals, fluid and melt inclusions by laser-ablation inductively-coupled-plasma mass-spectrometry. *Geochimica et Cosmochimica Acta* **67**, 3473–3496.

Herd, C. D. K. (2008). Basalts as probes of planetary interior redox state. In: McPherson, G. J., Mittlefehldt, D. W. & Jones, J. H. (eds) *Oxygen in the Solar System. Mineralogical Society of America and Geochemical Society, Reviews in Mineralogy and Geochemistry* **68**, 527–553.

Hildreth, W. & Wilson, C. J. N. (2007). Compositional zoning of the Bishop Tuff. *Journal of Petrology* **48**, 951–999.

Holland, T. J. B. & Powell, R. (1998). An internally consistent thermodynamic data set for phases of petrological interest. *Journal of Metamorphic Geology* **16**, 309–349.

Hu, Z., Gao, S., Liu, Y., Xu, J., Hu, S. & Chen, H. (2008). Niobium and tantalum concentrations in NIST SRM 610 revisited. *Geostandards and Geoanalytical Research* **32**, 347–360.

Isuk, E. E. & Carman, J. H. (1981). The system $Na_2Si_2O_5$–$K_2Si_2O_5$–MoS_2–H_2O with implications for molybdenum transport in silicate melts. *Economic Geology* **76**, 2222–2235.

Jochum, K. P., Stoll, B. *et al.* (2006). MPI-DING reference glasses for *in situ* microanalysis: New reference values for element concentrations and isotope ratios. *Geochemistry, Geophysics, Geosystems* **7**, Q02008, doi:10.1029/2005GC001060.

Jugo, P. J., Wilke, M. & Botcharnikov, R. E. (2010). Sulfur K-edge XANES analysis of natural and synthetic basaltic glasses: implications for S speciation and S content as function of oxygen fugacity. *Geochimica et Cosmochimica Acta* **74**, 5926–5938.

Keith, J. D., Shanks, W. C. I., Archibald, D. A. & Farrar, E. (1986). Volcanic and intrusive history of the Pine Grove porphyry molybdenum system, southwestern Utah. *Economic Geology* **81**, 553–577.

Keppler, H. & Wyllie, P. J. (1991). Partitioning of Cu, Sn, Mo, W, U and Th between melt and aqueous fluid in the systems haplogranite–H_2O–HCl and haplogranite–H_2O–HF. *Contributions to Mineralogy and Petrology* **109**, 139–150.

Lowenstern, J. B., Mahood, G. A., Hervig, R. L. & Sparks, J. (1993). The occurrence and distribution of Mo and molybdenite in unaltered peralkaline rhyolites from Pantelleria, Italy. *Contributions to Mineralogy and Petrology* **114**, 119–129.

Luhr, J. F. (2008). Primary igneous anhydrite: progress since its recognition in the 1982 El Chichón trachyandesite. *Journal of Volcanology and Geothermal Research* **175**, 394–407.

Manley, C. R. & Bacon, C. R. (2000). Rhyolite thermobarometry and the shallowing of the magma reservoir, Coso volcanic field, California. *Journal of Petrology* **41**, 149–174.

McCready, P. (2007). *Molybdenum. Mining Journal Supplementary.* London: Mining Communications Ltd, 16 p.

Pearce, J. A., Harris, N. B. W. & Tindle, A. G. (1984). Trace element discrimination diagrams for the tectonic interpretation of granitic rocks. *Journal of Petrology* **25**, 956–983.

Pettke, T. (2006). *In-situ* laser-ablation-ICP-MS chemical analysis of melt inclusion and prospects for constraining subduction zone magmas. In: Webster, J. D. (ed.) *Melt Inclusions in Plutonic Rocks. Mineralogical Association of Canada, Short Course Series* **36**, 51–80.

Pettke, T. (2008). Analytical protocols for element concentration and isotope ratio measurements in fluid inclusions by LA-(MC-) ICP-MS. In: Sylvester, P. J. (ed.) *Laser ablation ICP-MS in the Earth Sciences; Current Practices and Outstanding Issues. Mineralogical Association of Canada, Short Course Series* **40**, 189–217.

Rampino, M. R. & Self, S. (1992). Volcanic winter and accelerated glaciation following the Toba super-eruption. *Nature* **359**, 50–52.

Robie, R. A. & Hemingway, B. S. (1995). *Thermodynamic properties of minerals and related substances at 298·15 K and 1 bar (105 Pascals) pressure and at higher temperature. US Geological Survey Bulletin* **2131**, 456.

Rudnick, R. L. & Gao, S. (2003). The composition of the continental crust. In: Rudnick, R. L. (ed.) *The Crust, Treatise on Geochemistry, Vol. 3.* Oxford: Elsevier–Pergamon, pp. 1–64.

Shinohara, H., Kazahaya, K. & Lowenstern, J. B. (1995). Volatile transport in a convecting magma column: implications for porphyry Mo mineralization. *Geology* **23**, 1091–1094.

Simon, A. C., Candela, P. A., Piccoli, P. M., Mengason, M. & Englander, L. (2008). The effect of crystal–melt partitioning on the budgets of Cu, Au and Ag. *American Mineralogist* **93**, 1437–1448.

Sinclair, W. D. (2007). Porphyry deposits. In: Goodfellow, W. D. (ed.) *Mineral Deposits of Canada: a Synthesis of Major Deposit-types, District Metallogeny, the Evolution of Geological Provinces, and Exploration*

Methods. Geological Association of Canada, Mineral Deposits Division, Special Publication **5**, 223–243.

Stavast, W. J. A., Keith, J. D., Christiansen, E. H., Dorais, M. J., Larocque, A. & Evans, N. (2006). The fate of magmatic sulfides during intrusion or eruption, Bingham and Tintic Districts, Utah. *Economic Geology* **101**, 329–345.

Stimac, J. & Hickmott, D. (1994). Trace-element partition coefficients for ilmenite, orthopyroxene and pyrrhotite in rhyolite determined by micro-PIXE analysis. *Chemical Geology* **117**, 313–330.

Sun, S. S. & McDonough, W. F. (1989). Chemical and isotopic systematics of oceanic basalts: implications for mantle composition and processes. In: Saunders, A. D. & Norry, M. J. (eds) *Magmatism in the Ocean Basins. Geological Society, London, Special Publications* **42**, 313–345.

Tacker, R. C. & Candela, P. A. (1987). Partitioning of molybdenum between magnetite and melt: a preliminary experimental study of partitioning of ore metals between silicic magmas and crystalline phases. *Economic Geology* **82**, 1827–1838.

Tuttle, O. F. & Bowen, N. L. (1958). *Origin of Granite in the Light of Experimental Studies in the System $NaAlSi_3O_8$–$KAlSi_3O_8$–SiO_2–H_2O. Geological Society of America, Memoirs* **74**, 153.

Vazquez, J. A., Kyriazis, S. F., Reid, M. R., Sehler, R. C. & Ramos, F. C. (2009). Thermochemical evolution of young rhyolites at Yellowstone: evidence for a cooling but periodically replenished postcaldera magma reservoir. *Journal of Volcanology and Geothermal Research* **188**, 186–196.

Waldner, P. & Pelton, A. D. (2005). Thermodynamic modeling of the Fe–S system. *Journal of Phase Equilibria and Diffusion* **26**, 23–38.

Warshaw, C. M. & Smith, R. L. (1988). Pyroxenes and fayalites in the Bandelier Tuff, New Mexico—temperatures and comparison with other rhyolites. *American Mineralogist* **73**, 1025–1037.

Watson, B. E. & Harrison, M. T. (1983). Zircon saturation revisited: temperature and composition effects in a variety of crystal magma types. *Earth and Planetary Science Letters* **64**, 295–304.

Webster, J. D. (1997). Exsolution of a magmatic volatile phase from Cl-enriched mineralizing granitic magmas and implication for ore metal transport. *Geochimica et Cosmochimica Acta* **61**, 1017–1029.

Westra, G. & Keith, S. B. (1981). Classification and genesis of stockwork molybdenum deposits. *Economic Geology* **76**, 844–873.

Whitney, J. A. (1984). Fugacities of sulfurous gases in pyrrhotite-bearing silicic magmas. *American Mineralogist* **69**, 69–78.

Zajacz, Z., Halter, W. E., Pettke, T. & Guillong, M. (2008). Determination of fluid/melt partition coefficients by LA-ICPMS analysis of coexisting fluid and silicate melt inclusions: Controls on element partitioning. *Geochimica et Cosmochimica Acta* **72**, 2169–2197.

Zajacz, Z., Hanley, J. J., Heinrich, C. A., Halter, W. E. & Guillong, M. (2009). Diffusive re-equilibration of quartz-hosted silicate melt and fluid inclusions: are all metal concentrations unmodified? *Geochimica et Cosmochimica Acta* **73**, 3013–3027.

Zhu, L., Ding, Z., Yao, S., Zhang, G., Song, S., Qu, W., Guo, B. & Lee, B. (2009). Ore-forming event and geodynamic setting of molybdenum deposit at Wenquan in Gansu Province, Western Qinling. *Chinese Science Bulletin* **54**, 2309–2324.